Generation of Microwaves With Tuneable Frequencies in Ultracompact "Magnon Microwave Antenna" via Phonon-Magnon-Photon Coupling

Arindam Samanta, *Member, IEEE*, and Saibal Roy, *Member, IEEE*

***Abstract*— Here, we report a "magnon microwave antenna" (MMA) for the generation of microwaves with tuneable frequencies, based on modulation of confined spin waves (SWs) in the patterned array of magnetostrictive nanomagnets/piezoelectric heterostructures caused by the surface acoustic waves (SAWs). A SAW launched on a piezoelectric substrate produces a periodic strain within the nanomagnets patterned on it, which, in turn, stimulates magnetization precession resulting in different magneto-dynamical resonance modes in the array of nanomagnets with a rich SW texture. The generated SWs (magnons) further interact with the EM radiation (photons) at the SAW frequency. The phonon-magnon-photon coupling in the patterned array of nanowires (NWs) generates a 0.56 GHz microwave frequency with a 13.9 MHz linewidth and a *Q*-factor of 40, while that in a matrix of nanodots (having same overall area) provides tuneable frequencies leading up to 30 GHz with a linewidth of 59.1 MHz and an enhanced *Q*-factor of 439; having nonvolatile spin textures in both the cases. The generated nonvolatile spin textures of the NWs/nanodots can also be useful in energy-efficient logic and low-power computing applications.**

***Index Terms*— Magnon microwave antenna (MMA), microwave generation, phonon-magnon-photon coupling, piezoelectric/magnetostrictive heterostructure, spin torque oscillator (STO), spin wave (SW).**

I. Introduction

THE emergence of the Internet of Things (IoT) devices develops a great interest in microwave based technologies [1], [2], [3], in applications such as autonomous driverless/autopilot cars, efficient radars/antennae and so on, which rely on the generation of microwave frequencies with a relatively lower power consumption, strong signal amplitude, and good frequency stability. These high-end features become the prerequisite of the advanced systems to perform necessary operations smoothly. However, conventional voltage-controlled oscillators (VCOs) typically consume a large amount of power to perform the operations [4]. Previously, spin torque oscillators (STOs) have been investigated as a source of microwaves, as STOs are, in general, highly tuneable and offer small chip size compared to existing VCOs [5], [6], however, suffers from the weak output signal. To circumvent this issue, an array with synchronized phase-locking STOs has been studied. However, the synchronization time of such phase-locking STOs is extremely short, and in practical applications, the synchronization of the STOs itself becomes one of the biggest challenges, which limits their utilization for cutting-edge IoT applications. Additionally, some electric/magnetic field as an external bias is required in controlling the STOs [7], [8].

Lately, Fabiha et al. [9] used tripartite coupling between phonon-magnon-photon to demonstrate spin-wave (SW) based nano-antenna. In this work, we demonstrate, an SW-based "magnon microwave antenna" (MMA) for microwave generation via nonvolatile domain configuration induced by tripartite phonon-magnon-photon coupling in an array of magnetostrictive nanowires (NWs) patterned on a piezoelectric substrate. Since domains are modified at the cost of energy, here, the required energy has been provided to the NWs in the form of an external stress launched by a surface acoustic wave (SAW) in the piezoelectric substrate along the longitudinal direction. However, no external bias field is required as in other devices, e.g., STO-based or conventional domain wall-based oscillators or straintronic microwave oscillators [3], [10], [11], [12], [13], [14], [15], [16].

II. Results and Discussion

The proposed tripartite coupling based MMA consists of magnetostrictive NWs (FeGa) patterned on the piezoelectric $LiNbO_3$ substrate, which relies on two different working principles, first, phonon-magnon coupling and then the

Manuscript received 21 October 2022; accepted 7 November 2022. Date of publication 5 December 2022; date of current version 3 January 2023. This work was supported in part by the EU-H-2020 "EnABLES-JRA" Project under Grant 730957, in part by the Science Foundation Ireland (SFI) Principal Investigator (PI) Award Grant, and in part by the Frontiers for the Future Programme (FFP) Award Grant. The review of this article was arranged by Editor P. J. Fay. *(Corresponding author: Saibal Roy.)*

The authors are with the Micropower Devices/Systems and Nanomagnetics Group, Micro Nano Systems Centre, Tyndall National Institute, Cork T12R5CP, Ireland, and also with the Department of Physics, University College Cork, Cork T12YN60, Ireland (e-mail: saibal.roy@tyndall.ie).

Color versions of one or more figures in this article are available at https://doi.org/10.1109/TED.2022.3221026.

Digital Object Identifier 10.1109/TED.2022.3221026

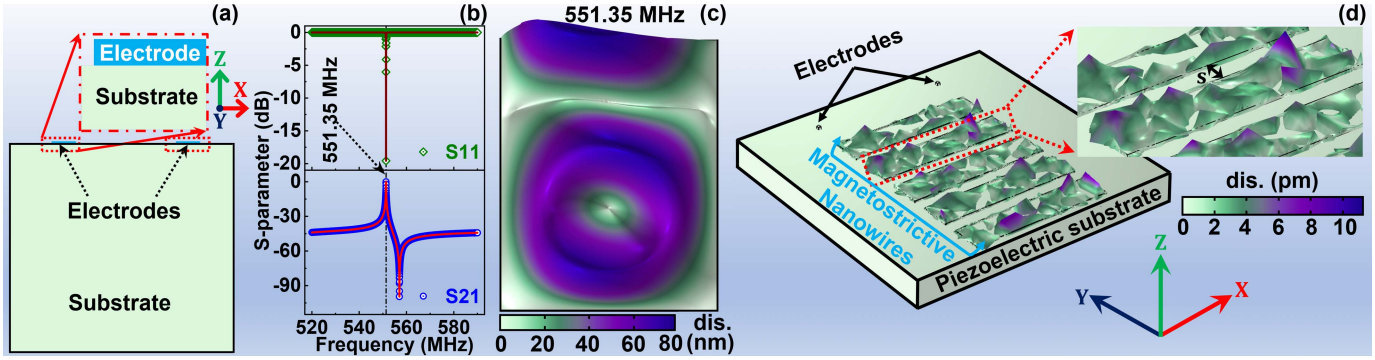

Fig. 1. COMSOL design of the MMA with magnetostrictive NWs. (a) 2-D cross-sectional model in COMSOL to calculate the generated SAW frequency. Substrate width −9 μm, thickness −10 μm; electrodes (the magnified version of the highlighted region) width −1 μm and thickness −5 nm. (b) S11 and S21 parameters confirm the SAW resonance frequency at 551.35 MHz. (c) Deformed shape plot of the resonance SAW mode confirms the maximum penetration depth of the SAW. (d) Magnetostriction effect in NWs shows some mechanical displacement of NWs caused by the SAW.

magnon-photon coupling. The following section first describes MMA design in a 2-D cross-sectional model with COMSOL[1] [17] [as in Fig. 1(a)] and then estimates the SAW resonance frequency generated from the system. In order to implement the necessary design and simulations, the piezoelectric effect and magnetostriction physics interfaces from the structural mechanics module along with the ac/dc module of COMSOL Multiphysics have been employed.

In the simulation, two of the electrodes separated by a distance of ∼3.6 μm and placed along the longitudinal direction of the substrate have been considered as terminal ports to apply voltage into the device for generating the SAW from the piezoelectric substrate. The reflection coefficients, namely, S11 and S21 parameters, as shown in Fig. 1(b), obtained from the COMSOL simulation estimate the SAW resonance frequency as 551.35 MHz. The orientation confirms that the generated SAW propagates along the longitudinal directions (i.e., X-direction). Thus simulated resonance frequency has been considered as input in micromagnetic simulation with MuMax^3 [18].

It is imperative to calculate the amount of power that is coupled to the SAW, which could be further utilized in the estimation of the stress generated upon launching of SAW. In order to do that, we have considered the similar approach by De et al. [19] and Drobitch et al. [20]. Here, the S11 parameter in Fig. 1(b) has been calculated considering an ideal scenario, i.e., any loss from the substrate has been neglected, that estimates the reflection coefficient of the system. The S11 value of ≈−19.56 dB gives the reflection coefficient (r) of the system as ≈0.011. Here, in the simulation, the input power (P_I) is 6.5 × 10^{-5} W. Therefore, the power coupled into the SAW is $P_C = (1 - r) \cdot P_I \approx 6.43 \times 10^{-5}$ W.

The corresponding stress profile at 551.35 MHz, generated due to SAW is shown in Fig. 1(c), which estimates the penetration depth on the surface as 80 nm. Hence, the thicknesses of the NWs should be smaller than 80 nm to ensure that all of the strain generated in the substrate due to the SAW is transferred to the NWs. Since the nanomagnet thickness in our study is 40 nm, it could be assumed that the generated strain has been transferred fully to the NWs producing the required magnetization, as confirmed in Fig. 1(d). The maximum mechanical displacement of the NWs caused by the strain from SAW is 10 pm. The following sections provide a deeper insight into the detailed magnetization study and the SW (magnonic) modes of MMA.

We have performed the micromagnetic simulations using MuMax^3 [18] by discretizing the NWs into the cell sizes of 2 × 2.5 × 2.5 nm solving the Landau–Lifshitz–Gilbert (LLG) equation [see (1) and (2)]. Here, $\vec{M}$ is the unit vector of local magnetization, $|\gamma|$ is gyromagnetic ratio (GHz/T), $\vec{H}_{\text{eff}}$ is the effective magnetic field originates from demagnetization energy, exchange energy, magnetic and shape anisotropy, α is the Gilbert damping factor, μ_0 is the free space permeability, M_S is the saturation magnetization (A/m)

$$\frac{\partial \vec{M}}{\partial t} = |\gamma|\vec{M} \times H_{\text{eff}} + \frac{\alpha}{M_S}\left[\vec{M} \times \frac{\partial \vec{M}}{\partial t}\right] \quad (1)$$

$$H_{\text{eff}} = -\frac{1}{\mu_0} \cdot \left[\frac{\partial E}{\partial \vec{M}}\right]. \quad (2)$$

We have considered the following material parameters of FeGa [21], saturation magnetization M_S = 1.32 MA/m, exchange stiffness constant A_{ex} = 16 pJ/m, initial exchange anisotropy constant $K_{u1,i}$ = 0 J/m^3, before applying external stress(σ). Since MuMax^3 does not include external stress directly [18], the stress has been applied as magnetoelastic anisotropy, $K_{\text{me}} = (3/2)\lambda_s \cdot \sigma(t)$, where λ_s is saturation magnetostriction constant of FeGa (400 ppm) and $\sigma(t)$ is the generated time-varying sinusoidal stress due to the launch of SAW [22]. So, the external stress reforms the uniaxial anisotropy value as $K_{u1,\text{eff}} = K_{u1,i} + K_{\text{me}}$ [21] $\Rightarrow K_{u1,\text{eff}} \approx (3/2)\lambda_s \cdot \sigma_0 \sin(2\pi f t)$ [22]. The stress field has further been calculated according to the following equation: $H_S(t) = (3/2) \cdot H_0 \cdot \sin(2\pi f t)$, where, $H_0 = ((\lambda_s \cdot \sigma_0)/(\mu_0 \cdot M_S))$ is the amplitude of the stress field ($H_S(t)$) due to SAW. Here, $\sigma_0 = (P_{A,\max} \cdot Z_{\max})^{1/2}$ and $Z_{\max} = (C_{\epsilon 11} \cdot \rho)^{1/2}$, where $Z_{\max}$, $C_{\epsilon 11}$ (202.897 × 10^9 Pa) and ρ (4.7 × 10^6 g/m^3) are characteristic acoustic impedance, the first diagonal element of the elasticity tensor and the density of the $LiNbO_3$ substrate, respectively. The power coupled into the SAW per unit area along the

[1]Registered trademark.

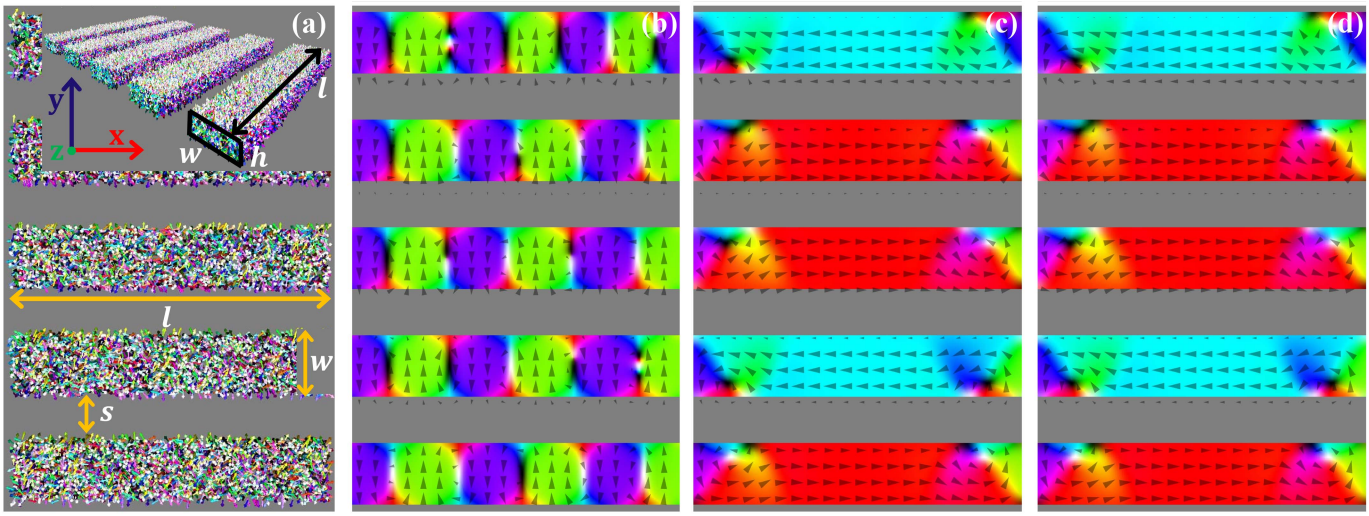

Fig. 2. Micromagnetic modeling of NWs. (a) Initial random magnetization configuration. *l*, *w* be the length and width of each of the NWs along the *x*- and *y*-directions, respectively, and *s* be the separation between the NWs along *y*-direction of 40 nm thick NWs. (b) Multidomain state in presence of transverse stress along *Y*. (c) Single domain state upon launching of the SAW along *X*. (d) Final spin configuration after completion of 20 ns simulation confirms that the domain configurations are nonvolatile in nature.

normal to the direction of propagation, $P_{A,\max} = P_C/A_{\max}$, where P_C is the power coupled into the SAW (6.43×10^{-5} W as calculated earlier) and $A_{\max}$ is the area (8×10^{-14} m^2) normal to the direction of propagation of the SAW [calculated as the width of the electrodes (1 μm) times the penetration depth of the SAW (80 nm)]. Therefore, $P_{A,\max}$ becomes 8×10^8 W/m^2, $Z_{\max} = 9.786 \times 10^8$ N·S/m^3 and $\sigma_0 = 1.25 \times 10^9$ Pa. Hence, the amplitude of $H_S(t)$, i.e., H_0 is 452 144 A/m = 5681 Oe.

Here, the cell size lies below exchange length ($l_{\text{ex}} = (2A_{\text{ex}}/\mu_0 M_S^2)^{1/2} \approx 4.24$ nm), which further ensures the inclusion of all of the exchange interactions. MuMax^3 determines the macro-spin configuration at every coordinate point within the NW and it produces the vector files containing the magnetization distribution over the simulating magnetic object. Simulations performed with the typical dimensions of NWs are $512 \times 120 \times 40$ nm [length(l) × width(w) × thickness(h)] as depicted in Fig. 2(a) with different "s" values (20–160 nm), where, we have considered the effective magnetic fields generated by the effect of the shape anisotropy, dipole coupling and strain. This study has been performed at 0 K, a widely used method in micromagnetic modeling of strain-mediated structures, to ignore the switching errors [23].

It is important to note that transverse stress applied along the *Y*-direction helps developing the multidomain configurations [as shown in Fig. 2(b)] along the cross section of the NWs out of initial random magnetization configuration [as shown in Fig. 2(a)]. Due to the SAW, the smaller multidomains in Fig. 2(b) start rotating into one direction in forming a large size single domain state along longitudinal direction [Fig. 2(c)], which helps to generate the microwaves. In the process of the creation or annihilation of domains, demagnetization energy has taken an important role. In general, the dipolar energy or demagnetizing energy of any system could be minimized by forming multiple domains in the system. Therefore, the energy should be minimized in the studied systems as well. We have considered our initial magnetization as random magnetization [Fig. 2(a)]. For s = 90 nm figuration, the demagnetization energy of the initial random magnetization state is 4484.20 aJ. The demagnetization energy becomes 818.32 aJ while the system has been broken into multidomain state [Fig. 2(b)]. The multidomain state has been diminished upon launching of the SAW. The energy associated with the SAW further helps to minimize the demagnetization energy of the system. In this case, the demagnetization energy of the single-domain state [Fig. 2(c)] is reduced to 337.83 aJ.

It is worth mentioning that such kind of change in domain wall motion with SAW is promising for wireless energy harvesting applications, such as for power-hungry IoT devices [24]. Another important aspect of our study is that the SAW-engineered single domain state is nonvolatile in nature, as evidenced in Fig. 1(d), after a 20 ns long simulation. These single-domain nanomagnets remain in its own state until they are reset by the application of stress or a strong external magnetic field to the initial multidomain state, which makes the single-domain state nonvolatile, that could be useful in energy-efficient logic applications, low-power computing applications, as well [25], however, that is out of the scope of the present study.

In electrically connected series or parallel STO [26], each of the individual NWs is connected through interdigitated electrodes delineated by lithography. However, the MMA provides the liberty to connect them without any electrical connection, rather they are connected via the dipolar interaction between them and the strength of the dipolar coupling could be considered analogous to the electrical resistance in the electrically connected STOs [26]. Since the SAW has been launched along the longitudinal (x) direction, the NWs could be considered to be connected magnetically in parallel combination via dipolar coupling between them as analogous to the electrical STOs and it is important to mention that the

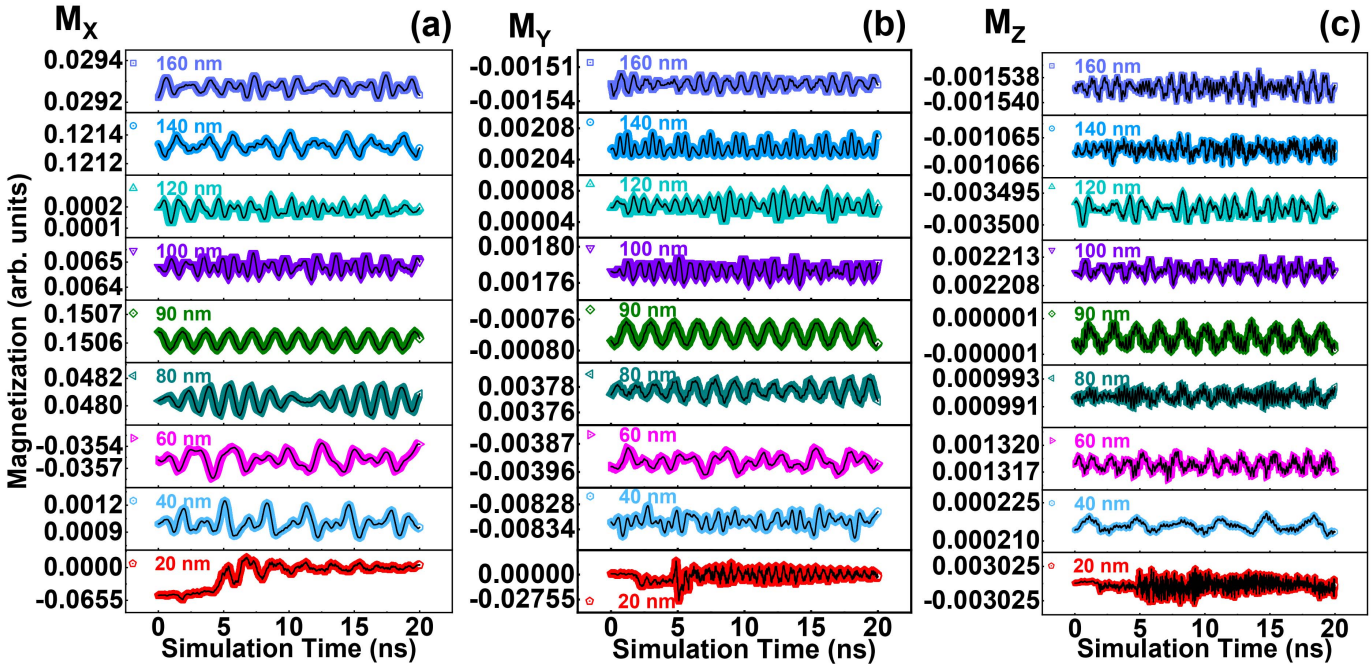

Fig. 3. Calculated magnetization oscillations as a function of the spacing between the NWs in MMA along *x*-, *y*-, and *z*-directions in (a)–(c), respectively, while the exciting SAW frequency remains kept constant at 0.5 GHz throughout the simulations.

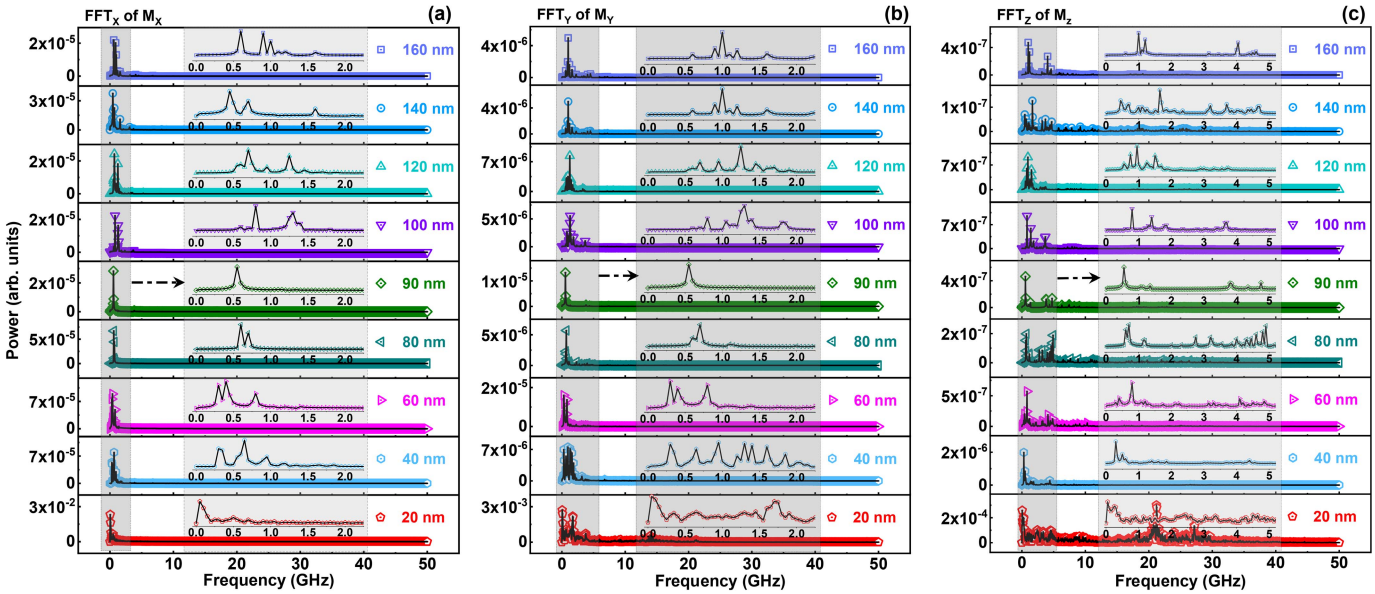

Fig. 4. Power distribution as a function of spacing between the NWs along *x*-, *y*-, and *z*-directions in (a)–(c), respectively. The corresponding insets reveal the magnified frequency spectra (0–2.5(5) GHz range) of M_X and M_Y (M_Z) of the highlighted region at left side of the parent power-frequency spectra (0–50 GHz range).

demagnetization energy along with the exchange energy plays a crucial role in stabilizing the magnetization oscillations. So, there must be a trade off between the demagnetization energy and the exchange energy of the systems. Therefore, it is important to note that in the absence of the SAW, the system might excite at its intrinsic SW mode due to strong magnetostatic interaction between the neighboring elements and/or in presence of SAW, new extrinsic modes might occur at the SAW frequencies which are not resonant with the intrinsic modes [19].

We have shown the calculated magnetization components, M_X, M_Y, and M_Z, as a function of the increasing separation value ("*s*") between the NWs in Fig. 2(a)–(c), respectively, where M_X, M_Y, and M_Z represent the calculated magnetization components along the major, minor axes and normal to the plane component of the NW, respectively. To find the optimum separation for effective synchronization, the SAW with 0.5 GHz frequency has been launched first, as obtained from the COMSOL simulation shown in Fig. 1(b). Both the configurations with the smallest and largest separations

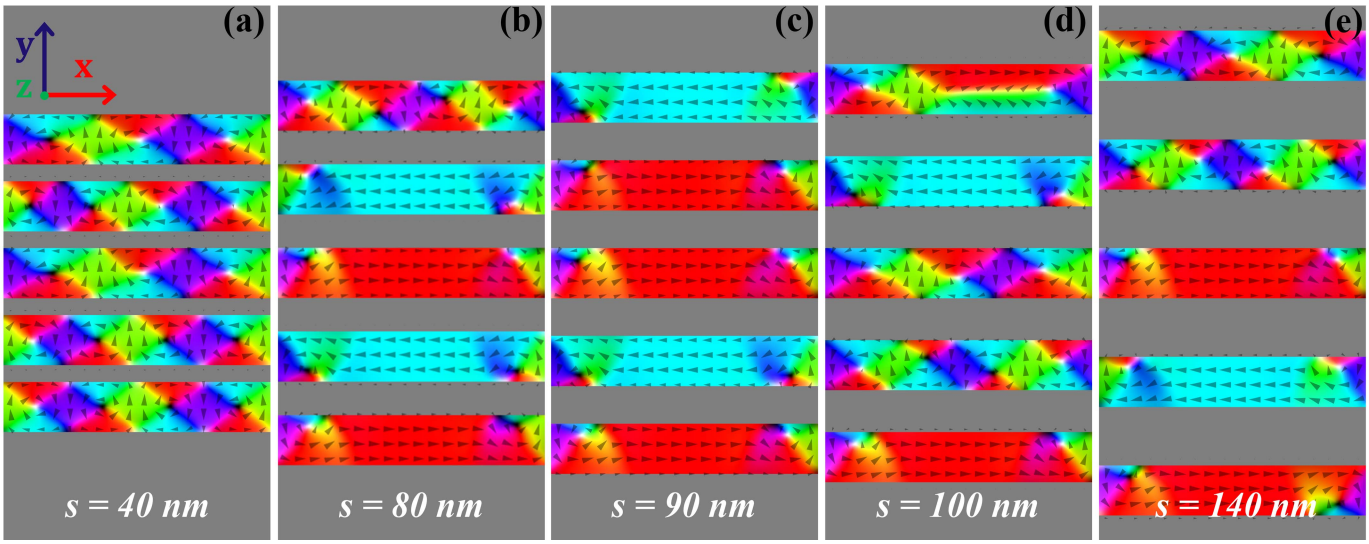

Fig. 5. (a)–(e) Final spin configuration of the NWs after completion of 20 ns of micromagnetic simulation showing the nonvolatility nature of the domains for the separation values, 40, 80, 90, 100, and 140 nm, respectively.

between the NWs, i.e., 20 and 160 nm, give desynchronized oscillations in all the directions, i.e., along the x-, y-, and z-directions, respectively, as evidenced in Fig. 3(a)–(c). Hence, these configurations have failed to generate properly synchronized auto-oscillations in the microwave antenna, which has been evidenced by the multiple peaks in the corresponding fast Fourier transform (FFT) spectra, in Fig. 4(a)–(c), of the corresponding damped magnetization curves, respectively. However, the configuration with moderate separation, i.e., the NWs separated with 90 nm distance, provides the required optimum magnetization output (M_X and M_Y) with properly synchronized auto-oscillations, i.e., an undamped sinusoidal response along x- and y-directions, respectively. In addition, the sinusoidal M_Z component in this configuration seems to be suffered from slight damping. It is important to notice that the magnetization oscillation amplitudes decrease almost by one order of magnitude from M_X to M_Z.

The FFT of the magnetization components, M_X, M_Y, M_Z yields the corresponding power spectra of each configuration. The obtained power-frequency spectra of $M_X/M_Y/M_Z$ by FFT as a function of "s" value between the NWs are shown in Fig. 4(a)–(c), respectively. The corresponding insets in each stack show the magnified frequency spectra of the highlighted region of the parent power spectra (0–50 GHz range). The $s = 20$ nm configuration shows only a single peak in FFT_X (the power is in 10^{-2} order of magnitude), however, any effect from the SAW might be absent as its magnetization is noisy, and not synchronized in any direction at all, as evidenced in Fig. 4(a)–(c). At this configuration, the intrinsic shape anisotropy and the strength of the magnetostatic interaction are more prominent [overall demagnetization energy (∼297 aJ) is greater than the exchange energy (∼200 aJ)] that obstruct to synchronize with the launched SAW frequency and trigger incoherent magnetization precession inside the nanomagnets and hence the power is concentrated at low frequency (that is the natural frequency of the system), which arises due to the array geometry itself [19].

For $s = 40$ nm configuration, there are four peaks in the corresponding spectrum, which means that at least two NWs are synchronized along x-direction. However, the power at this configuration becomes three orders of magnitude smaller (the power is in 10^5 order of magnitude) than that in 20 nm configuration, as in the case of 40 nm configuration, the exchange energy (∼375 aJ) dominates over the demagnetizing energy of the system. As a result, new extrinsic modes generate upon launching of SAW.

Upon increasing the separation between the NWs, some of the peaks start merging as the number of peaks is decreased as depicted in Fig. 4. For $s = 60$ nm, there are three different peaks, which necessarily signifies that at least three NWs are synchronized. For $s = 80$ nm, the number of the synchronized NWs is four, however, the $s = 90$ nm configuration generates only a single frequency where each of the five NWs is properly synchronized giving rise to the optimum output. Here, we denote this synchronized frequency for $s = 90$ nm configuration as the "peak frequency," f_p, and the "s" value as s_{op}, i.e., the optimum separation value for effective synchronization of each of the NWs. Upon further increasing the separation value destroys the synchronized state as evidenced in Fig. 4. In addition, the power-frequency spectra along the minor direction also show a similar kind of behavior, i.e., only $s = 90$ nm separation gives a proper synchronized signal along y-direction. So, it could be mentioned that the frequency response is identical along the major and minor directions, respectively, i.e., the MMA could be exploited bidirectionally for required applications. However, the magnitude in FFT_Y becomes almost half of that in FFT_X.

On the other hand, FFT_Z in Fig. 4(c) confirms that it is extremely hard to synchronize the NWs at any separation value studied here in the out-of-plane (Z) direction; even the s_{op} configuration has some other weaker (power) higher bands (frequency) over f_p. The time-varying strain generated in the magnetostrictive nanomagnet due to the SAW modulates

the overall precessional dynamics, which in turn give rise to the hybrid magnetodynamical modes along out-of-plane component [27] and this might be the reason behind the higher band along z-direction. Here, the power of the resonance peak, "f_p" of M_X is approximately two (six) times larger than that of M_Y (M_Z) oscillations. Hence, the SW is composed mostly of the longitudinal oscillations in the component of the magnetization along the major axis while the SAW is also propagating along the same direction.

Domains of all these studied phonon-magnon-photon coupling based MMAs are observed to be nonvolatile in nature (as shown in Fig. 2). However, it is imperative to mention that there is a significant difference in the nonvolatility of the domains for different separation values, as shown in Fig. 5(a)–(e). For example, domains of all of the NWs for s = 40 nm configuration are organized in a diamond orientation, while for s = 80 nm, domains of one NW are found in such a diamond orientation, as shown in Fig. 5(a) and (b), respectively. Similarly, diamond domain orientations are found in several NWs for s = 100/140 nm configurations as shown in Fig. 5(d) and (e), respectively. However, for s = 90 nm configuration, a single domain with the aforementioned nonvolatile configurations is found as shown in Fig. 5(c), which might be the possible reason behind synchronization of all of the NWs and providing only a single peak output frequency, where efficient coupling between the launched SAW (phonon) and generated SW (magnon) has occurred.

The calculated phase and power profiles (at s = 90 nm configuration) of the SWs at the dominant peak frequency (i.e., 0.55 GHz) are shown in Fig. 6(a) and (b), respectively (obtained after post-processing of the magnetization data with python). The phase profile shows that the profile at the 0.55 GHz frequency is almost uniform, while the power profile at this frequency exhibits a complex propagation mode in longitudinal direction. Therefore, the power in the SW at s = 90 nm configuration is mostly concentrated in the longitudinal magnetization oscillations.

In order to obtain the tuneability, we further patterned the array of NWs in the MMA by keeping s_{op} unaltered at 90 nm along the transverse direction to develop a matrix of nanodots in the MMA with 25 elements of dimensions 90 × 120 nm separated at a horizontal distance of 15 nm as shown in Fig. 7. Fig. 7(a) shows the initial random magnetization configuration of the matrix of nanodots constituting the MMA, each of which becomes a multidomain state, as shown in Fig. 7(b) upon applying transverse stress in the matrix [previously, we observed similar effects for the NWs in the MMA as in Fig. 2(b)]. After launching the SAW on the substrate, the multidomain states transform into multivortex states, as shown in Fig. 7(c). Interestingly, it is observed, as shown in Fig. 7(d), that the matrix of nanodots in the MMA retains their initial multivortex state (that has been obtained after launching the SAW on the substrate) even after completion of 20 ns of simulation demonstrating their nonvolatility nature.

Due to further patterning of the NWs in MMA as shown in Fig. 7(a), instead of generating the mutually synchronized auto-oscillations in the NWs, the magnetization auto-oscillations in the nanodots along x-/y-/z-directions

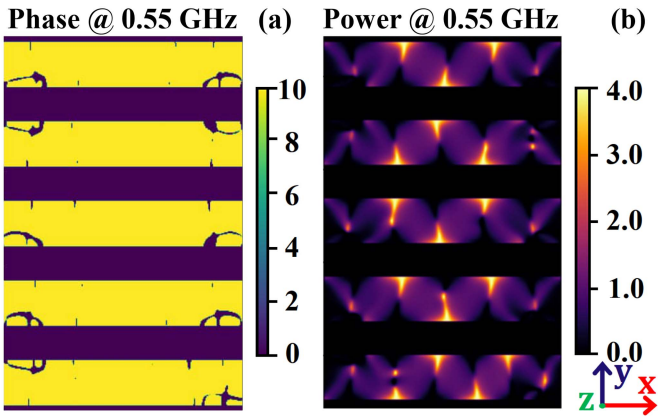

Fig. 6. At s = 90 nm configuration, (a) Phase and (b) power profiles of the SWs at the dominant frequency, i.e., the 0.55 GHz mode showing the uniformity of the profile, and complex propagation mode in longitudinal direction, respectively. The color bars are shown on the right side of each of the figures.

become nonlinear with time and exhibit a quasi-stable fluctuation as evidenced from Fig. 8(a)–(c), respectively. The M_X component has a prominent beating period of ∼6 ns. This nonlinear auto-oscillation generates 1.5/1.4 GHz microwave frequencies as shown in FFT_X/FFT_Y in Fig. 9(a) and (b) along with some other bands (4.8 GHz in FFT_X or 6.3 GHz in FFT_Y) with smaller amplitudes along the x- and y-directions, respectively. However, the FFT_Z as shown in Fig. 9(c) shows a multiband (1.4–30 GHz) frequency spectra, where both the 27.25 and 4.8 GHz frequencies have almost the same amplitudes.

It is also worth mentioning that the generated frequencies are greater than the SAW frequency, i.e., the nano-matrix has its own magnonic modes due to the rich SW properties, which are determined by the exchange energy and the demagnetizing energy. The exchange energy in this matrix of nanodots in the MMA (393 aJ) is almost double than the NWs of MMA (187 aJ), while the demagnetization energy of the matrix of nanodots in the MMA (238 aJ) becomes smaller than that of the NWs of MMA (337 aJ). So, there must be a trade off between the demagnetization energy and the exchange energy of the systems. In the latter case, the unique frequency tunability seems to be governed by the particular exchange coupling modification in the vicinity of each of the dots within the nano-matrix in the MMA. Overall, depending upon the requirement, this novel ultracompact MMA could be designed to generate desired frequencies and the generated nonvolatile spin textures of the NWs/nanodots can also be useful in energy-efficient logic and low-power computing applications.

The generated SWs further radiate electromagnetic waves (photons) into the surrounding space, which could be captured with a horn-antenna/spectrum analyzer for desired applications [20]. The phonons, due to the launched SAW on the piezoelectric substrate, first get coupled into the generated magnons within the nanomagnets and following that, the magnons further couple into the photons, i.e., the tripartite coupling between phonon-magnon-photon takes place, which could be exploited to generate desired microwave frequencies.

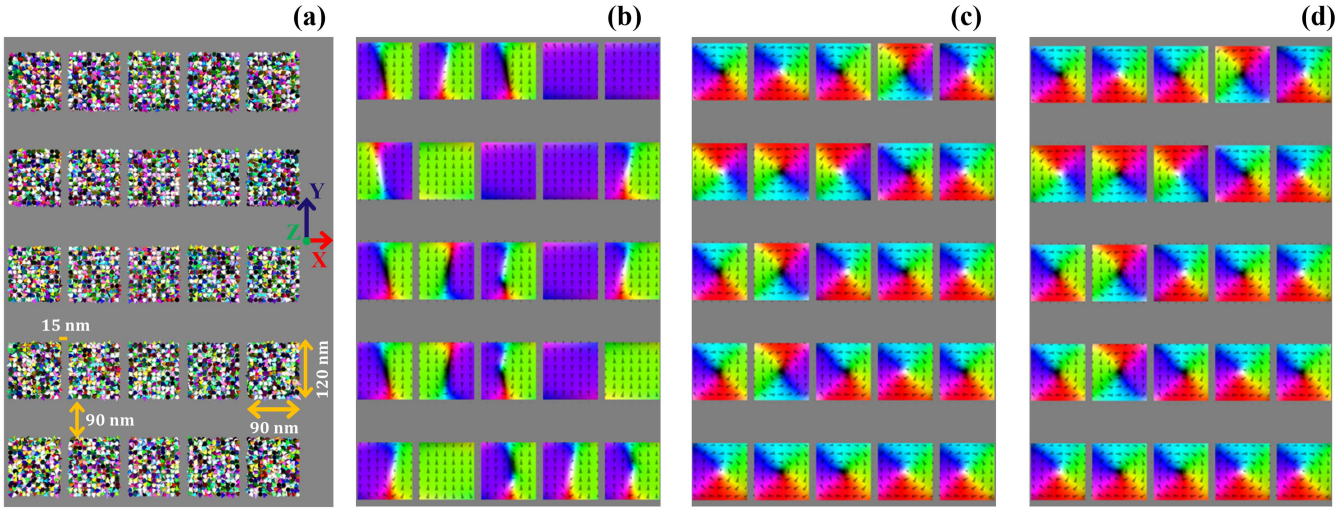

Fig. 7. Micromagnetic modeling of the patterned matrix of nanodots in the MMA. (a) Initial random magnetization configuration of the arrays. (b) Obtained multidomain configuration in each of the nanodots in presence of transverse stress along *Y*-direction. (c) Multidomain structures in (b) are diminished upon launching of the 0.5 GHz SAW along *X*-direction. (d) Final spin configuration of the NWs after completion of 20 ns simulation showing the nonvolatility nature of the domains.

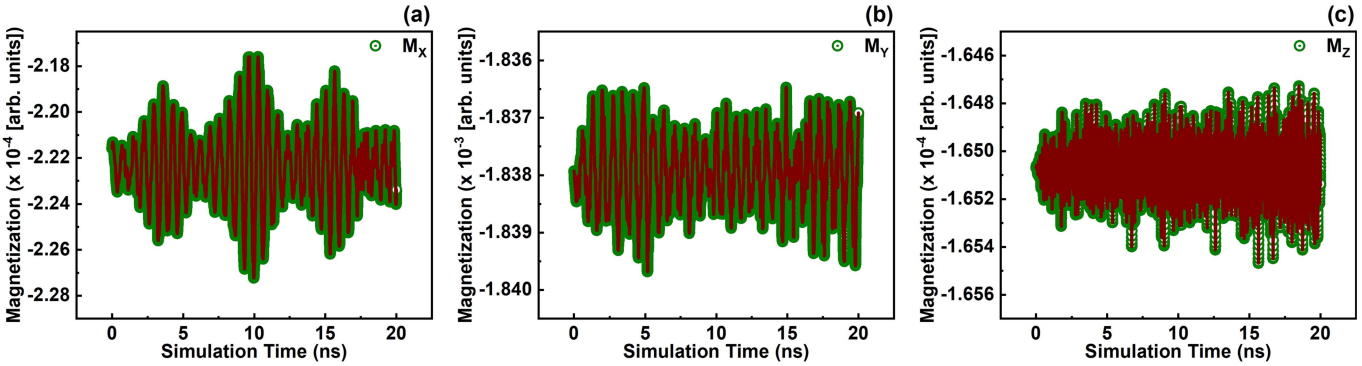

Fig. 8. Calculated oscillations in the magnetization components, M_X, M_Y, and M_Z, in a matrix of nanodots in the MMA along *x*-, *y*-, and *z*-directions in (a)–(c), respectively, while the exciting SAW frequency remains kept constant at 0.5 GHz throughout the simulations.

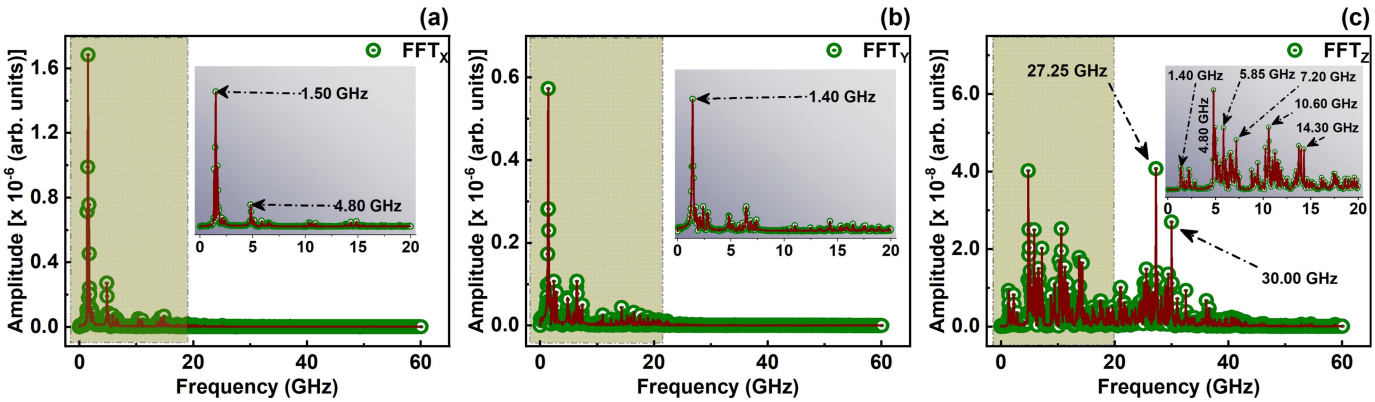

Fig. 9. Power distribution of the patterned matrix of nanodots in the MMA along *x*-, *y*-, and *z*-directions in (a)–(c), respectively. In each of the graphs, the corresponding insets reveal the magnified frequency spectra (0–20 GHz range) of M_X, M_Y, and M_Z of the highlighted region on the left side of the parent power-frequency spectra (0–60 GHz range).

III. Conclusion

In conclusion, we have investigated a tripartite coupling between phonons (SAW), magnons (SW), and photons (EM wave) in ultracompact SW-dependent MMA developed with magnetostrictive NWs/nanodots on the piezoelectric substrate while generating microwaves with tuneable frequencies. Initially, SAW is launched onto the piezoelectric substrate, which stimulates the magnetization precession of the NWs/nanodots. As a result, the magnons (SW) have been generated within the NWs/nanodots, which in turn causes the radiation of EM

waves into the surroundings. The generated radiation can be collected by a horn antenna for applications. Hence, these MMAs are based on the tripartite coupling which provides an advantage to utilize themselves over the electromechanical resonance-based antennas. In addition, this novel structure gives the liberty to further miniaturize the overall existing size of the devices.

Acknowledgment

Author Contributions: Arindam Samanta performed the COMSOL and micromagnetic simulations. Arindam Samanta took a major role in analyzing the data and writing the draft of the manuscript in conjunction with Saibal Roy. The authors conceived the idea. Saibal Roy designed the project to bring the necessary research grant, and supervised Arindam Samanta for his Ph.D. dissertation. Arindam Samanta wishes to thank Bhadri Narayanan of Tyndall National Institute for help in initial COMSOL simulations.

Competing Interests: The authors declare no competing interests.

Data Availability

The data that support the findings of this study are available from the corresponding author upon reasonable request.

References

[1] H. Harada and M. Fujise, "Feasibility study on a highly mobile microwave-band broad-band telecommunication system," *IEEE Trans. Intell. Transp. Syst.*, vol. 3, no. 1, pp. 75–88, Mar. 2002.

[2] K. Huang and X. Zhou, "Cutting the last wires for mobile communications by microwave power transfer," *IEEE Commun. Mag.*, vol. 53, no. 6, pp. 86–93, Jun. 2015.

[3] S. Bhatti and S. N. Piramanayagam, "High amplitude microwave generation using domain wall motion in a nanowire," *Phys. Status Solidi, Rapid Res. Lett.*, vol. 13, no. 3, Mar. 2019, Art. no. 1800479. [Online]. Available: https://onlinelibrary.wiley.com/doi/abs/10.1002/pssr.201800479

[4] F. Chicco, A. Pezzotta, and C. C. Enz, "Analysis of power consumption in LC oscillators based on the inversion coefficient," in *Proc. IEEE Int. Symp. Circuits Syst. (ISCAS)*, May 2017, pp. 1–4.

[5] Q. Mistral et al., "Current-driven microwave oscillations in current perpendicular-to-plane spin-valve nanopillars," *Appl. Phys. Lett.*, vol. 88, no. 19, 2006, Art. no. 192507, doi: 10.1063/1.2201897.

[6] D. Kumar et al., "Coherent microwave generation by spintronic feedback oscillator," *Sci. Rep.*, vol. 6, no. 1, Nov. 2016, Art. no. 30747, doi: 10.1038/srep30747.

[7] D. A. Allwood, G. Xiong, C. C. Faulkner, D. Atkinson, D. Petit, and R. P. Cowburn, "Magnetic domain-wall logic," *Science*, vol. 309, no. 5741, pp. 1688–1692, Sep. 2005. [Online]. Available: https://science.sciencemag.org/content/309/5741/1688

[8] J. Åkerman, "Toward a universal memory," *Science*, vol. 308, no. 5721, pp. 508–510, Apr. 2005. [Online]. Available: https://science.sciencemag.org/content/308/5721/508

[9] R. Fabiha, J. Lundquist, S. Majumder, E. Topsakal, A. Barman, and S. Bandyopadhyay, "Spin wave electromagnetic nano-antenna enabled by tripartite phonon-magnon-photon coupling," *Adv. Sci.*, vol. 9, no. 8, Mar. 2022, Art. no. 2104644. [Online]. Available: https://onlinelibrary.wiley.com/doi/abs/10.1002/advs.202104644

[10] R. Sbiaa, M. A. Bahri, and S. N. Piramanayagam, "Domain wall oscillation in magnetic nanowire with a geometrically confined region," *J. Magn. Magn. Mater.*, vol. 456, pp. 324–328, Jun. 2018. [Online]. Available: https://www.sciencedirect.com/science/article/pii/S0304885317332900

[11] M. Voto, L. Lopez-Diaz, and E. Martinez, "Pinned domain wall oscillator as a tuneable direct current spin wave emitter," *Sci. Rep.*, vol. 7, no. 1, p. 13559, Dec. 2017, doi: 10.1038/s41598-017-13806-1.

[12] B. Van de Wiele, S. J. Hämäläinen, P. Baláž, F. Montoncello, and S. van Dijken, "Tunable short-wavelength spin wave excitation from pinned magnetic domain walls," *Sci. Rep.*, vol. 6, no. 1, p. 21330, Feb. 2016, doi: 10.1038/srep21330.

[13] A. Samanta and S. Roy, "Generation of high amplitude microwaves in nanowires induced by domain wall motion," in *Proc. 15th Joint MMM-Intermag Conf.*, Jan. 2022, p. 432. [Online]. Available: https://magnetism.org/wp-content/uploads/sites/82/2022/04/2022-Joint_MMM-Intermag-FINAL-WEB.pdf#page=433

[14] A. Dec and K. Suyama, "Microwave MEMS-based voltage-controlled oscillators," *IEEE Trans. Microw. Theory Techn.*, vol. 48, no. 11, pp. 1943–1949, Nov. 2000.

[15] S. M. Mohseni et al., "High frequency operation of a spin-torque oscillator at low field," *Phys. Status Solidi, Rapid Res. Lett.*, vol. 5, no. 12, pp. 432–434, Dec. 2011. [Online]. Available: https://onlinelibrary.wiley.com/doi/abs/10.1002/pssr.201105375

[16] M. A. Abeed, J. L. Drobitch, and S. Bandyopadhyay, "Microwave oscillator based on a single straintronic magnetotunneling junction," *Phys. Rev. Appl.*, vol. 11, no. 5, May 2019, Art. no. 054069. [Online]. Available: https://link.aps.org/doi/10.1103/PhysRevApplied.11.054069

[17] COMSOL AB. (2022). *COMSOL Multiphysics Version 6.0*. [Online]. Available: https://www.comsol.com

[18] A. Vansteenkiste, J. Leliaert, M. Dvornik, M. Helsen, F. Garcia-Sanchez, and B. Van Waeyenberge, "The design and verification of MuMax^3," *AIP Adv.*, vol. 4, no. 10, Oct. 2014, Art. no. 107133, doi: 10.1063/1.4899186.

[19] A. De, J. L. Drobitch, S. Majumder, S. Barman, S. Bandyopadhyay, and A. Barman, "Resonant amplification of intrinsic magnon modes and generation of new extrinsic modes in a two-dimensional array of interacting multiferroic nanomagnets by surface acoustic waves," *Nanoscale*, vol. 13, no. 22, pp. 10016–10023, Jun. 2021, doi: 10.1039/D1NR01177D.

[20] J. L. Drobitch et al., "Extreme subwavelength magnetoelastic electromagnetic antenna implemented with multiferroic nanomagnets," *Adv. Mater. Technol.*, vol. 5, no. 8, 2020, Art. no. 2000316. [Online]. Available: https://onlinelibrary.wiley.com/doi/abs/10.1002/admt.202000316

[21] D. Bhattacharya, M. M. Al-Rashid, N. D'Souza, S. Bandyopadhyay, and J. Atulasimha, "Incoherent magnetization dynamics in strain mediated switching of magnetostrictive nanomagnets," *Nanotechnology*, vol. 28, no. 1, Nov. 2016, Art. no. 015202, doi: 10.1088/0957-4484/28/1/015202.

[22] M. S. Fashami, J. Atulasimha, and S. Bandyopadhyay, "Magnetization dynamics, throughput and energy dissipation in a universal multiferroic nanomagnetic logic gate with fan-in and fan-out," *Nanotechnology*, vol. 23, no. 1, Feb. 2012, Art. no. 105201, doi: 10.1088/0957-4484/23/10/105201.

[23] Z. Xiao et al., "Bi-directional coupling in strain-mediated multiferroic heterostructures with magnetic domains and domain wall motion," *Sci. Rep.*, vol. 8, no. 1, p. 5207, Dec. 2018, doi: 10.1038/s41598-018-23020-2.

[24] S. Bhatti, C. Ma, X. Liu, and S. N. Piramanayagam, "Stress-induced domain wall motion in FeCo-based magnetic microwires for realization of energy harvesting," *Adv. Electron. Mater.*, vol. 5, no. 1, 2019, Art. no. 1800467. [Online]. Available: https://onlinelibrary.wiley.com/doi/abs/10.1002/aelm.201800467

[25] V. Sampath, N. D'Souza, D. Bhattacharya, G. M. Atkinson, S. Bandyopadhyay, and J. Atulasimha, "Acoustic-wave-induced magnetization switching of magnetostrictive nanomagnets from single-domain to nonvolatile vortex states," *Nano Lett.*, vol. 16, no. 9, pp. 5681–5687, 2016, doi: 10.1021/acs.nanolett.6b02342.

[26] R. Sharma et al., "Electrically connected spin-torque oscillators array for 2.4 GHz WiFi band transmission and energy harvesting," *Nature Commun.*, vol. 12, p. 2924, May 2021, doi: 10.1038/s41467-021-23181-1.

[27] S. Mondal et al., "Hybrid magnetodynamical modes in a single magnetostrictive nanomagnet on a piezoelectric substrate arising from magnetoelastic modulation of precessional dynamics," *ACS Appl. Mater. Interfaces*, vol. 10, no. 50, pp. 43970–43977, 2018, doi: 10.1021/acsami.8b19243.